RESEARCH ARTICLE | MARCH 19 2025

High-voltage current sensing with nitrogen-vacancy centers in diamond

Shao-Chun Zhang; Long Zhao; Ru-Jia Qiu; Jia-Qi Geng; Teng Tian; Bo-Wen Zhao; Yong Liu ; Long-Kun Shan ; Xiang-Dong Chen; Guang-Can Guo ; Fang-Wen Sun

APL Photonics 10, 036117 (2025)
https://doi.org/10.1063/5.0256419

High-voltage current sensing with nitrogen-vacancy centers in diamond

Cite as: APL Photon. 10, 036117 (2025); doi: 10.1063/5.0256419
Submitted: 4 January 2025 • Accepted: 27 February 2025 •
Published Online: 19 March 2025

Shao-Chun Zhang,[1,2] Long Zhao,[3] Ru-Jia Qiu,[3] Jia-Qi Geng,[1,2,3] Teng Tian,[3] Bo-Wen Zhao,[4] Yong Liu,[1,2] Long-Kun Shan,[1,2] Xiang-Dong Chen,[1,2,5,a)] Guang-Can Guo,[1,2,5] and Fang-Wen Sun[1,2,5,b)]

AFFILIATIONS

[1] CAS Key Laboratory of Quantum Information, University of Science and Technology of China, Hefei 230026, People's Republic of China
[2] CAS Center For Excellence in Quantum Information and Quantum Physics, University of Science and Technology of China, Hefei 230026, People's Republic of China
[3] Electric Power Quantum Sensing Joint Laboratory of Anhui Province, State Grid Anhui Electric Power Research Institute, Hefei 230601, China
[4] Anhui Guosheng Quantum Technology Co., Ltd., Hefei 230088, China
[5] Hefei National Laboratory, University of Science and Technology of China, Hefei 230088, China

[a)] **Electronic mail:** xdch@ustc.edu.cn
[b)] **Author to whom correspondence should be addressed:** fwsun@ustc.edu.cn

ABSTRACT

The negatively charged nitrogen-vacancy color center in diamond exhibits several remarkable properties, which make it widely used in magnetic field sensing. In particular, the magnetic field measurements can be traced back to frequency, which makes diamond sensors promising for high-precision current measurement. Here, we develop a quantum current transformer (QCT) with four fiberized diamond sensors uniformly toroidally distributed in a magnetic shielding loop. We proposed fluorescence signal treatments of frequency-doubled conversion and weighted averaging under a zero bias magnetic field, which can reconstruct the 50 Hz alternating-current waveform. A maximum accuracy of 0.05% for AC amplitude measurements is achieved over a highly linear range of 0–1000 A. In addition, tracing two resonance frequencies simultaneously enabled the suppression of temperature drift in the current measurement. Finally, we apply this QCT to current monitoring in a 110 kV substation, verifying its practicality in the power supply network. Such a QCT can provide a robust and scalable platform for current quantum sensing technologies for high-voltage power transmission while reducing the complexity of operation and maintenance.

I. INTRODUCTION

Current sensing is widely used in power supply networks to transmit and distribute electrical energy at high voltage (HV).[1] The reliability and accuracy of high-voltage current measurement (HVCM) are significant requirements for HV current mode control, energy saving, and protection purposes.[2,3] Various HVCM technologies are currently available and appropriate for HV applications, such as Ohm's law-shunt resistors,[4] optical sensors based on the Faraday effect,[5] and magnetic field sensors based on tunnel magnetoresistance.[6] However, with the large-scale development of HV or ultra-HV power supply networks, broadband oscillation and harmonic resonance of the power networks will become serious, making these traditional measurement methods difficult to meet the requirements for high-precision measurement in a wide current and temperature range.[7]

Quantum sensing has garnered increasing interest for its potential to realize unprecedented sensitivity for magnetic field sensing.[8] Various systems, such as superconducting quantum interference devices (SQUIDs),[9] atomic vapor cells,[10] and solid-state spins,[11] have been proposed for quantum sensors. The negatively charged nitrogen-vacancy (NV) color center in diamond[12] enables linear

responsibility up to an 8 T magnetic field[13] and ambient operation conditions up to 1000 K temperature.[14] These make NV color centers become one of the most promising platforms for magnetic field sensing with sub-nanotesla sensitivities[15] and bandwidths of up to ~100 kHz.[16] Typically, the diamond-based magnetic field sensors can recognize and respond to current circuits, which can be used in current density imaging[17,18] and neuronal current detection[19,20] on a micrometer scale. Diamond sensors developed on a millimeter scale have been demonstrated in high-current laboratory applications, such as high-precision direct current (DC) measurement with a magnetic yoke[21–23] and power management of electric vehicles.[24] However, the saturation magnetization effect will narrow the current range, and the instability of the bias magnetic field and even the hysteresis effect will also introduce systematic errors.[3] These factors challenge diamond sensors to achieve reliable and accurate HVCM.

To address these problems, we developed a quantum current transformer (QCT) loop with four fiberized diamond sensors uniformly toroidally distributed based on Ampere's circuit law. With the [100] crystal orientation of each diamond parallel to the magnetic field generated by the conductor, the signal-to-noise ratio (SNR) of optically detected magnetic resonance (ODMR) can be improved. In this case, we proposed fluorescence signal treatments of frequency-doubled conversion and weighted averaging for four fiberized diamond sensors, which can accurately reconstruct the 50 Hz alternating-current (AC) waveform. In addition, we used a fixed-frequency method for magnetic field measurement, and its dynamic range can be broadened by shifting the microwave frequency. We achieved a maximum current measurement accuracy of 0.05% for the AC amplitude over a highly linear range of 0–1000 A. Finally, we applied this QCT for current monitoring in an outdoor 110 kV substation, verifying its practicality in the power supply network. Theoretically, the current measurement by QCT can be traced back to the clock frequency, promising to enable remote calibration or self-calibration. Such a QCT can provide a high-precision current measurement method for high-voltage power transmission and reduce the complexity of operation and maintenance.

II. EXPERIMENTAL DESIGN

A. HVCM experimental setup

Benefiting from their compactness and technical robustness, fiberized diamond-based sensors have been demonstrated for magnetometers.[25–29] Here, a fiberized HVCM schematic is shown in Fig. 1(a). In the experiment, a 532 nm green pump laser is first split by 99:1, and the small part is monitored and adjusted by a homemade proportional-integral-derivative controller to stabilize another part of laser power. Then, the laser is divided equally into four channels and finally coupled into the multi-mode optical fibers (details are shown in Appendix A). Four fiberized diamond-based sensors are uniformly toroidally distributed in a magnetic shielding loop. This can suppress the impact of the external magnetic fields and the slight eccentricity of the conductor on the current measurement accuracy. The NV center spin state-dependent pho-

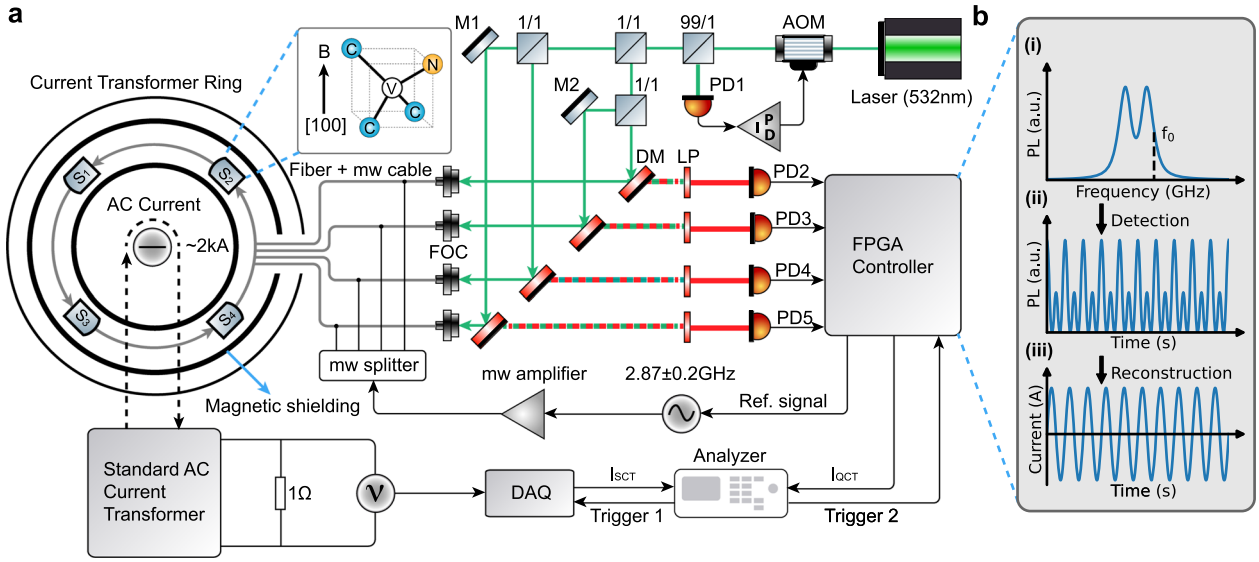

FIG. 1. Schematic of the HVCM experimental setup and AC measurement method. (a) Four fiberized diamond sensors (S_1–S_4) are evenly distributed in a magnetic shielding loop, and the [100] crystal orientation is parallel to the magnetic field generated by the current. Bulk diamonds are coupled to the end face of multimode optical fibers, and laser excitation and fluorescence collection are achieved through the same optical fiber. PID (proportional-integral-derivative) technology stabilizes the laser power, evenly dividing it into four beams as pump light for the diamond sensors. A self-developed FPGA controller can achieve fluorescence signal modulation, acquisition, and processing. Finally, a standard current transformer performs current measurement synchronously and compares it with the diamond-based methods in real-time. PD, photodetector. DAQ, data acquisition card. AOM, acousto-optic modulator. DM, dichroic mirror. LP, long pass filtering. FOC, fiber optic coupler. (b) Magnetic field measurement and AC reconstruction process of fixed-frequency method.

toluminescence is collected by the same fiber and detected by a photodetector. A homemade Field Programmable Gate Array (FPGA) controller is applied to modulate the microwave, demodulate the fluorescence signal of four fiberized diamond sensors, and finally reconstruct the current. A standard current transformer (SCT) with an accuracy of 0.02% performs the current detection simultaneously. It is important to note that the SCT can convert a large current into a small one, which is ultimately detected by an acquisition card (NI, USB-6002). By synchronously comparing the current measurement results of QCT and SCT in real-time, the performance of the QCT can be determined, including accuracy, range, linearity, etc.

The diamond sample we used is a [100]-cut electronic grade sample grown using chemical vapor deposition, containing a natural (1.1%) abundance of ^{13}C and an NV concentration of 3.7 ppm. The NV center is a C_{3v} symmetric color center in a diamond formed by substituting a nitrogen atom adjacent to a vacancy in the carbon lattice. It has an electronic spin-triplet (S = 1) ground state with a zero-field splitting at room temperature of D ≈ 2.87 GHz between the $|m_s = 0\rangle$ and $|m_s = \pm 1\rangle$ sublevels. An external magnetic field will split the $|m_s = \pm 1\rangle$ sublevels by the Zeeman effect. We align the [100] crystal orientation of each diamond parallel to the AC magnetic field B_{ac} generated by the conductor. In this case, B_{ac} projects equally onto all four NV symmetry axes, splitting the $|m_s = 0\rangle \rightarrow |m_s = \pm 1\rangle$ transitions equally. As a result, all the NV centers contribute to the ODMR spectrum, and the SNR can be improved.

B. Experimental protocol and data analysis

In the presence of a magnetic field B_z, the NV ground-state Hamiltonian is given by

$$H = (D_{\mathrm{zfs}} + \Pi_z)S_z^2 + (B_z + A_{zz}I_z)S_z - \Pi_x(S_x^2 - S_y^2) + \Pi_y(S_xS_y + S_yS_x), \quad (1)$$

where the electron gyromagnetic ratio $\gamma_e \approx 2.8$ MHz/G, and $A_{zz} = 2.16$ MHz, $D_{\mathrm{zfs}} \approx 2.87$ GHz is the zero-field splitting. $\hat{z}$ is the NV axis, and $\hat{x}$ is defined such that one of the carbon-vacancy bonds lies in the x–z plane. $S_{x,y,z}$ and I_z are the electronic spin-1 operators of NV and nuclear spin-1 operators of the host ^{14}N, respectively. The terms $\Pi_{x,y,z}$ characterize the coupling between NV and the strain-electric field. $B_z = B_{z0} + k_{cal}I_0\cos(\omega t + \phi)$ represents the axial magnetic field, where B_{z0} is the external static magnetic field, and k_{cal} is the linear factor derived from the Biot–Savart law. For the ground state transition frequencies, we have

$$f_{\pm} = D_{\mathrm{zfs}} + \Pi_z \pm \sqrt{\Pi_x^2 + \Pi_y^2 + (B_z + m_I A_{zz})^2}, \quad (2)$$

where $m_I = \{-1, 0, +1\}$.

Figure 1(b) schematically demonstrates the reconstruction of a 50 Hz current signal by lock-in optically detected magnetic resonance (ODMR) technology. The lock-in ODMR spectrum can be defined as a sum of Lorentzian distributions with six transition frequencies $\sum_{\pm,m_I} C\gamma^2/(\gamma^2 + \Delta^2)$, where $\Delta = f_0 - f_{\pm}$ is the MW frequency detuning. In general, the linear region with the maximum ODMR slope [where the center frequency is f_0 as depicted in Fig. 1(b-i)] has the strongest response to magnetic field variations. In this case, when fixing the MW frequency at f_0, the lock-in signal can be given by $S_{lock-in} \propto |\Delta|$. Since the detuning Δ does not depend linearly on the magnetic field B_z, the sinusoidal waveform of the AC magnetic field cannot be directly reconstructed through $S_{lock-in}$, as shown in Fig. 1(b-ii). Mathematically, we can square $S_{lock-in}$ and Fourier expand it as

$$S_{lock-in}^2(t) = a_0 + a_1\cos(\omega t + \phi_1) + a_2\cos(2\omega t + \phi_2) + a_3\cos(3\omega t + \phi_3) + \cdots. \quad (3)$$

This fluorescence signal treatment can eliminate the square root in Eq. (2), and then the 100 Hz frequency-doubled signal will dominate. By recording $S_{lock-in}^2$ for 0.2 s of about 10 cycles of the waveform, the amplitude a_2 and phase ϕ_2 of 100 Hz can be obtained in real-time. Theoretically, assuming that the current measurement result of SCT is the absolute value and a_2 is the output value of QCT, we can finally get the current response function by using SCT and QCT synchronously for current sensing,

$$a_2 = f(I_0). \quad (4)$$

Once we extract a_2 and ϕ_2 from Eq. (3), the AC waveform of the CH-i sensor can be reconstructed as

$$I_{0,i} = f_i'(a_2)\cos(\omega t + \phi_2/2), \quad (5)$$

as shown in Fig. 1(b-iii). In this case, the amplitude and phase information of the 50 Hz AC magnetic field can be accurately measured. Note that although all four fiberized diamond sensors contribute to the current measurement, the differences in sensor manufacture and installation result in inconsistent measurement errors. We can weigh the four current outputs ($I_{0,i}$) and average them, so the final current measurement result is obtained by

$$I = \sum_{i=1}^{4} w_i I_{0,i}, \quad (6)$$

where w_i is the error weighting factor, which linearly depends on the ODMR signal-to-noise ratio.

III. RESULTS

A. Current measurement response functions

The zero-field ODMR spectra of four channels (CH1–CH4) are shown in Fig. 2(a). As it is difficult to ensure the consistency of homemade sensing probes, such as the pump laser or microwave power, the linewidth and contrast of the ODMR spectra differ. However, constructing a current calibration function can compensate for its influence on the current measurement accuracy. Hereafter, we keep the MW frequency fixed at 2.885 GHz, and the 0.2 s experimental time-traces $S_{lock-in}$ of CH1 under different amplitudes of 50 Hz AC are shown in Fig. 2(b). Due to the inability of linearly polarized microwaves to selectively excite two resonances, we cannot distinguish the direction of current.[30,31] Therefore, these non-sinusoidal traces indicate that the ODMR signal is nonlinear with the magnetic field when using the fixed-frequency method. Theoretically, the fluorescence time traces as a function of the AC amplitude can be simulated via Eq. (3), which is in good agreement with the experimental results. To reconstruct the alternating current, we square $S_{lock-in}$ via Eq. (3). This results in higher harmonics of 50 Hz in

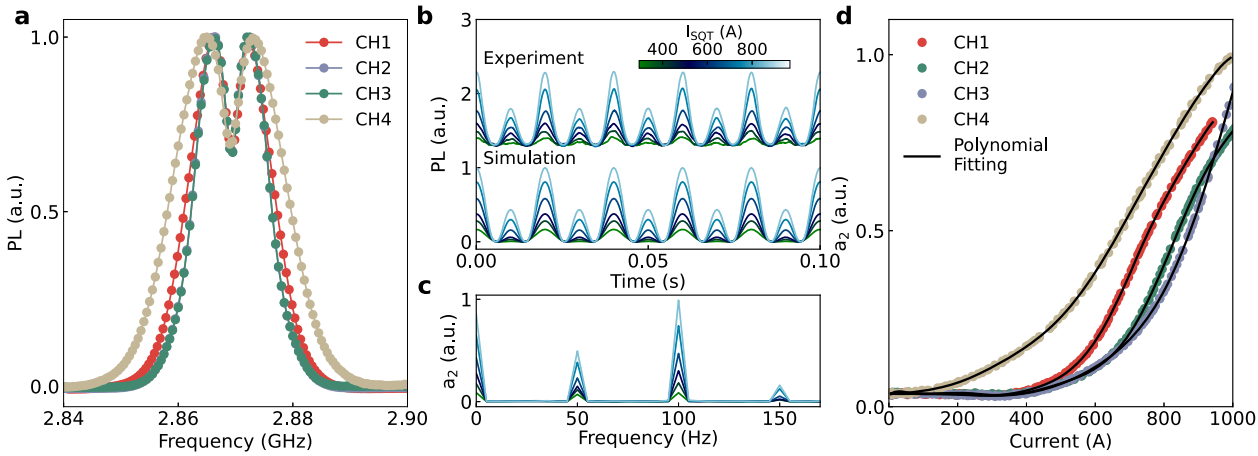

FIG. 2. AC measurement based on ODMR detection. (a) ODMR spectra of the four fiberized diamond sensors. Note that the two curves of CH2 and CH_3 almost overlap. (b) The lock-in output for different amplitudes of 50 Hz AC. They are in good agreement with the simulation. (c) The Fast Fourier Transform (FFT) results for experimental time traces in (b), where the 100 Hz component is dominant. (d) By extracting the 100 Hz component as a function of AC amplitude, the response functions of four channels can be obtained by polynomial fitting of at least sixth order.

$S^2_{lock-in}$, especially the dominant 100 Hz component a_2, as shown in Fig. 2(c). By extracting the a_2 as a function of current amplitude I_0 from SCT, the calibration functions $f^{-1}(a_2)$ of four channels can be obtained by a polynomial fitting of at least sixth order, as shown in Fig. 2(d). In this case, we can perform the AC measurement according to the process depicted in Fig. 1(b).

B. Current measurement dynamic range broadening

Since the current measurement dynamic range of the fixed-frequency method is limited by the ODMR linewidth, the current reconstructed via Eq. (4) shows nonlinearity with the magnetic field. This results in that only the region of maximum responsivity and near linearity (700–900 A) is available for current measurement. In this case, the current value of a single channel can be obtained by Eq. (5) as demonstrated in Subsection II B. Generally, such a data treatment can be realized by an FPGA controller, but the complex calibration function calculation is time-consuming and computationally intensive. Experimentally, we converted the non-analytical calibration function into 2^{16} sets of mapping arrays based on the sampling accuracy (16 bits) of the analog-to-digital converter (ADC), and then saved them in FPGA. Once a_2 is demodulated, the current value I can be obtained by looking up the table. This process takes less than 10 μs. Finally, we weight the current value I by Eq. (6) to further improve the measurement accuracy.

The accuracy of the current measurement is given by $\eta = \delta S/(IdS/dI)$, where the standard deviation of the sensor signal δS is compared to the response of the system dS in a changing current amplitude dI. For the HVCM using parameter demodulation and amplitude calibration, the accuracy is written as

$$\eta = \frac{\delta a_2}{I_0 f'(I_0)}. \tag{7}$$

Here, the standard deviation δa_2 is dominated by the shot noise of the fluorescence signal, and the current variation responsivity $f'(I_0)$ is laser and microwave power dependent. Experimentally, keeping the laser power constant, the response function of different microwave powers is shown in Fig. 3(a). The response function becomes steeper with increasing microwave power over the current dynamic range of 700–900 A, leading to the diamond sensor being more sensitive to the magnetic field variation. As a result, all current measurements are performed at maximum microwave power output (15 dbm). On the other hand, this dynamic range is significantly limited when fixing the microwave frequency. The accuracy of measuring small current amplitudes (usually below 10% of the rated current) will be reduced. To address it, we match the microwave frequency to nearly resonate with the NV spins, then the diamond sensor becomes more sensitive to the magnetic field variations. This can shift the dynamic range to cover the weak current measurements, as shown in Fig. 3(b). However, this method faces the challenges of predicting the trend of current amplitude changes and rapidly switching microwave frequencies. Ideally, tracking the spin resonance frequency by a closed-loop frequency-locked technique with fast frequency hopping can easily achieve a wider dynamic range,[32,33] as discussed in Appendix B.

Before dwelling on the accuracy of current measurements, it is necessary to analyze magnetic field sensitivity. Without applying the current, we keep the microwave frequency at the maximum slope of ODMR (on-resonance) and then continuously record the output $S_{lock-in}$ for 100 s. By calculating and averaging the amplitude spectral density (ASD) per second, the magnetometer sensitivity can be obtained by $\eta_B = \delta S/(k\gamma_e \cos\theta)$. Here, the gyromagnetic ratio γ_e = 28 GHz/T, δS is the ASD output of the lock-in amplifier, k is the maximum slope of ODMR, and $\theta \approx 54.5°$ is the angle between the magnetic field and the NV axis. For comparison, the ASD trace of off-resonance is also investigated, as shown in Fig. 3(c). For CH1,

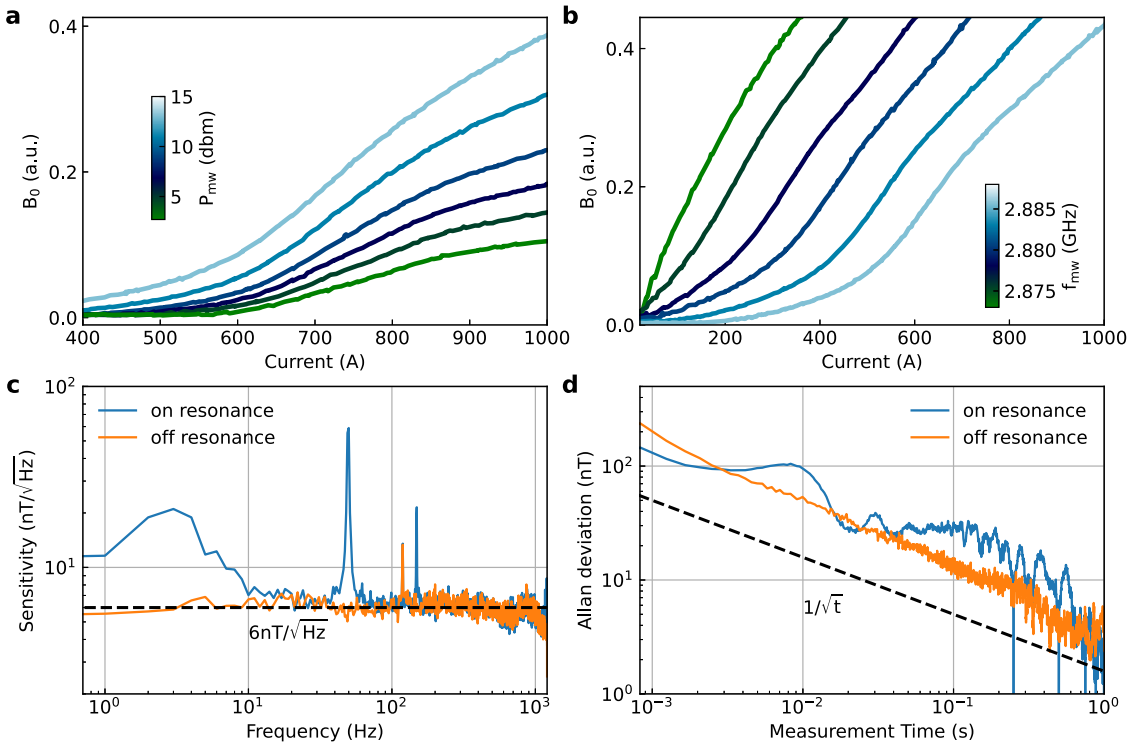

FIG. 3. Optimize current measurement performance. (a) Response functions of CH1 with different microwave power. Note that the maximum microwave power output is 15 dBm. (b) Response functions of CH1 with different microwave frequencies f_0 illustrated in Fig. 1(b-i). The current measurement dynamic range can be broadened by shifting the microwave frequencies. (c) Plots of the magnetic noise spectral density when on-resonance and off-resonance. The sensitivity is 6 nT/$\sqrt{\text{Hz}}$ with a bandwidth from 1 to 1400 Hz. The peaks highlight the detection of the 50 Hz magnetic hum and its second odd harmonic. (d) Plots of the Allan deviation of the traces in (c). The trends show drops scaling with $\tau^{-1/2}$, highlighting the dominance of white noise in this regime.

we finally obtain a sensitivity of 6 nT/$\sqrt{\text{Hz}}$ and a wide frequency bandwidth from 1 Hz to 1.4 kHz. On the other hand, Allan deviation can provide information on the correlation of consecutive measurements without being affected by overall long-term drift, as depicted in Fig. 3(d). As a result, the best magnetic field resolution can be realized for a measurement time of about 1 s. No further improvement by averaging is achieved.

C. Current measurement accuracy and analysis

We now turn to the current measurement. We first obtained the calibration functions of different dynamic measurement ranges. Then, we perform the current measurement by QCT in the 0–1000 A range and compare it with SCT, as shown in Fig. 4(a). Unlike the nonlinear response using the fixed frequency method shown in Fig. 2(c), the dashed line in Fig. 4(a) is the linear fitting of the response function after the real-time dynamic range shift. Figure 4(a-i) illustrates an enlarged display of the 690A current measurement result, and the data points are evenly distributed around the fitting curve. Figure 4(a-ii) shows the real-time synchronous recording of QCT and SCT. It can be seen that QCT can accurately and quickly respond to fluctuations in the current amplitude. In this case, we can use $\delta_e = |I_{QCT} - I_{SCT}|/I_{SCT}$ to obtain the relative error of the current measurement, and its statistical distribution is shown in Fig. 4(b). By Gaussian fitting, we realized a measurement accuracy of 0.05%. The accuracies within 1000 A are shown in Fig. 4(c). Theoretically, the statistical error of QCT is constant, which depends only on the system noise (such as fluorescent shot noise, thermal noise, etc.). This leads to the current measurement accuracy being inversely proportional depending on the current amplitude to be measured. However, in practical applications, accuracy is often compromised by system instabilities—such as drifts in laser/microwave power—which alter the calibration function of current measurements, ultimately reducing overall precision. In addition, the QCT's nonlinear error is defined as $\delta_L = |\Delta L_{\max}|/R$, where $\Delta L_{\max}$ is the largest difference between the data points and the fitting curve, and R is the dynamic range. From Fig. 4(c), $\Delta L_{\max}$ can be estimated to be ~1.68 A, and we can obtain a nonlinear error of 0.16%. Finally, we developed the above technology into current measurement equipment and installed it in a 110 kV substation, as shown in Appendix A for details. The QCT performed real-time monitoring of the current waveform of one channel in a three-phase AC circuit, verifying the feasibility of QCT's technical route.

Nevertheless, since the transmission efficiency of lasers in multimode optical fibers can be easily affected by vibration and temperature drift, the current measurement accuracy is difficult to maintain

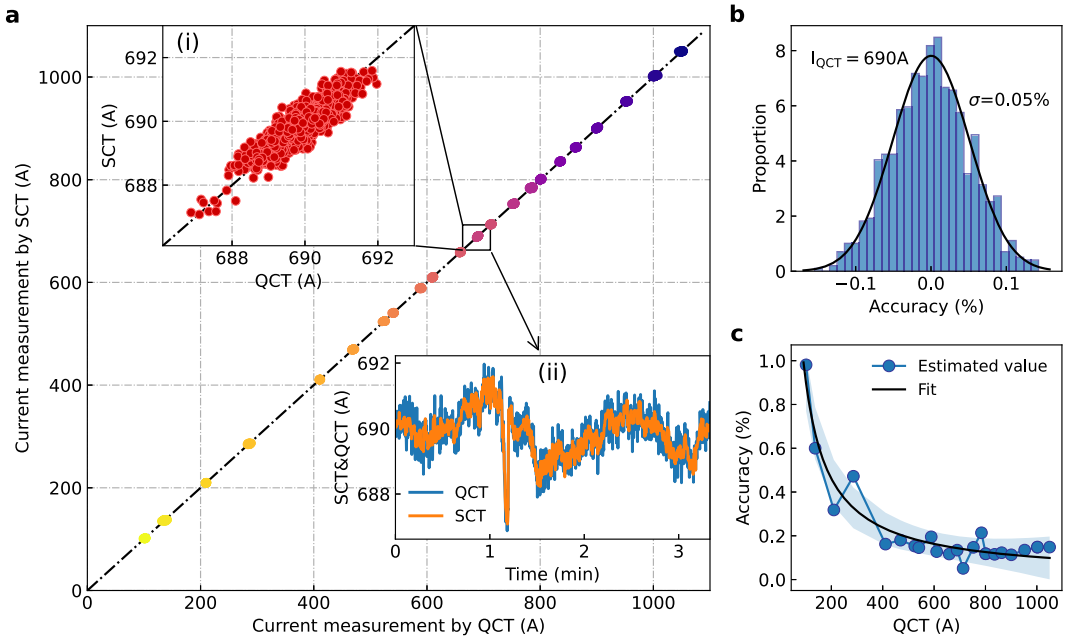

FIG. 4. Demonstrations of the current measurement accuracy. (a) The SCT and QCT are used to measure ACs with amplitudes of 100–1000 A synchronously. By shifting the MW frequency, linearity and dynamic range can be effectively improved. (i) illustrates the enlarged display of the 690 A current measurement result. (ii) is the real-time synchronous recording of QCT and SCT. (b) shows the error distribution of the 690 A current measurement, where we obtain an optimal accuracy of 0.05% by Gaussian fitting. (c) is the accuracies within 1000 A, which are fitted by inverse proportionality.

long-term stability. However, we can use dual-frequency quantum control methods to eliminate the temperature drift,[34,35] as demonstrated in Appendix C. In addition, using PID real-time feedback with fast switching of microwave frequency, we can also achieve fast tracking of spin resonance frequency.[32,33] This will suppress the impact of laser and microwave power drifts on current measurement accuracy. The heterogeneous integration of light sources, diamonds, photodetectors, etc., can realize fiber-free diamond magnetic sensors and avoid the influence of optical fiber vibration.[36–38] To further improve the current measurement accuracy, a zero flux closed-loop feedback method can be used. By applying feedback current, the magnetic sensor always works in a zero magnetic state.[39,40] In addition, to suppress the decrease in accuracy caused by eccentricity, the position variations of the conductor can be inverted through vector magnetic measurement of the quantum sensor array.[41,42] Ultimately, the multi-channel diamond magnetometer can be developed into a distributed quantum fiber magnetometer,[43] which can further expand the number of probes and improve the robustness of current measurement.

IV. CONCLUSION AND OUTLOOK

In conclusion, we evenly distributed four fiberized diamond sensors in a magnetic shielding loop and finally demonstrated a high-precision AC measurement device. The key to this device is measuring the alternating magnetic field under zero bias. In this architecture, the diamond [100] axes of all sensors are parallel to the magnetic field generated by the current, which can increase the signal-to-noise ratio of the ODMR spectrum. The response function of a specific detection current interval can be obtained using the fixed microwave frequency method. Moreover, shifting the microwave frequency can also widen the current measurement range. Finally, we obtained a maximum current measurement accuracy of 0.05% and a linearity of 0.16% in the range of 0–1000 A. These results support the application potential of high-voltage current measurement.

In addition, the current measurement accuracy can be further improved by enhancing the fluorescence collection efficiency and purifying ^{12}C;[44] the latter can narrow the zero-field ODMR spectrum and significantly improve its sensitivity to changes in current or magnetic field. While employing frequency tracking technology, diamonds with a [111] crystal orientation are preferable. This orientation simplifies aligning the external magnetic field parallel to the NV center axis, ensuring a linear relationship between the NV center resonance frequency and the measured current or magnetic field. This linearity enhances measurement precision and simplifies signal interpretation. This diamond-based sensor can also be applied to DC measurements. These techniques provide a compatible, minimally invasive approach for power metering, equipment status detection, and safety of long-distance power transmission.

ACKNOWLEDGMENTS

This work was supported by the Innovation Program for Quantum Science and Technology (Grant No. 2021ZD0303200), the CAS Project for Young Scientists in Basic Research (Grant No. YSBR-049), the National Natural Science Foundation of China (Grant Nos. 62225506, U23B20114, 62305324, 12005218, and 52130510),

and the Key Research and Development Plan of Jiangsu Province (Grant No. BE2022066-2). The sample preparation was partially conducted at the USTC Center for Micro and Nanoscale Research and Fabrication.

AUTHOR DECLARATIONS

Conflict of Interest

The authors have no conflicts to disclose.

Author Contributions

Shao-Chun Zhang: Conceptualization (equal); Data curation (equal); Formal analysis (equal); Writing – original draft (equal). **Long Zhao**: Investigation (equal). **Ru-Jia Qiu**: Formal analysis (equal). **Jia-Qi Geng**: Data curation (equal). **Teng Tian**: Data curation (equal). **Bo-Wen Zhao**: Investigation (equal). **Yong Liu**: Investigation (equal). **Long-Kun Shan**: Investigation (equal). **Xiang-Dong Chen**: Conceptualization (equal); Data curation (equal); Formal analysis (equal). **Guang-Can Guo**: Conceptualization (equal); Data curation (equal). **Fang-Wen Sun**: Conceptualization (equal); Data curation (equal); Formal analysis (equal); Writing – review & editing (equal).

DATA AVAILABILITY

The data that support the findings of this study are available from the corresponding author upon reasonable request.

APPENDIX A: DEMONSTRATION APPLICATION OF QCT IN OUTDOOR SUBSTATION.

The outer side of the sensor loop in QCT is an aluminum shell with outer and inner diameters of 68.6 and 40.4 cm. The inner side is a pair of loops made of silicon steel sheets with 60.4 and 50 cm diameters (with a thickness of 2 cm), respectively. This structure can shield against the interference of external environmental magnetic field fluctuations. The diamond sensor is installed between these silicon steel sheets. The sensor includes a coupling optical fiber, ferrule clamps, and a microwave antenna, which are integrated and assembled through a 3D-printed support. The optical fiber is a multimode fiber with a diameter of 200 μm and a numerical aperture of 0.37, clamped by a post-mountable nonmagnetic ferrule (Thorlabs, FCM13/M). The microwave antenna is a coplanar waveguide antenna with a center frequency close to 2.87 GHz;[45] its high radiation efficiency greatly reduces the requirement for strong microwave power. A small bulk diamond with a size of $200 \times 200 \times 100$ μm^3 is attached to the end of the fiber and placed in the central radiation area of the antenna. The [100] crystal direction of the diamond is perpendicular to the antenna surface. Aligning the antenna perpendicular to the tangent of the sensing loop results in only one pair of peaks appearing in the ODMR spectrum.

Subsequently, to verify the applicability of QCT in outdoor working environments, we finally installed the developed QCT in a substation with a voltage level of 110 kV and monitored the single-channel current in the three-phase AC. The sensor loop was installed at the bottom of the outdoor insulator (the rated AC passing through it was nearly 600 A), and the host chassis was installed indoors. The two were connected by four almost 30 m optical fiber and microwave cables, which were arranged underground to avoid fluorescent noise caused by cable vibration. Figure 5 shows the reconstructed current waveform via Eq. (5) in real-time.

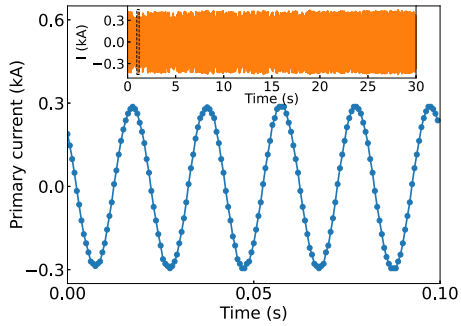

FIG. 5. Data are acquired for 0.1 s at the sampling rate of 1.6 ksamples/s, which shows a sine waveform with an amplitude of about 300 A at 50 Hz. The inset shows the data acquired for 30 s.

APPENDIX B: DEMONSTRATE THE APPLICATION OF FREQUENCY TRACKING TECHNOLOGY

The previously developed fixed-frequency method hardly limits the current measurement dynamic range. To widen it, we propose a frequency-tracking method to make the linear response range cover all the currents to be measured. Although we have achieved a current measurement range of 1000 A, we still face many challenges in breaking through the range and bandwidth limitations. For example, the simultaneous fast switching of microwave frequencies and calibration functions requires a signal conditioning delay of less than 100 μs. On the other hand, when the dynamic range limited by the ODMR linewidth is smaller than the magnetic field deviation caused by the AC, the response of the diamond to large currents will be reduced. Therefore, developing a real-time resonance frequency tracking technology is necessary to reconstruct the magnetic field. We can finally calculate the current 50 Hz AC amplitude and phase more accurately by calibration function inversion.

To demonstrate the feasibility of frequency-tracking technology for current measurement, we built an electromagnetic platform in the laboratory to simulate the real current measurement in the electricity network. A small current is applied to the solenoid to generate a magnetic field parallel to the [100] axis of the diamond. First, we linearly scan the current in the solenoid from −0.2 to 0.2 A with a step of 1 mA and record the ODMR spectra of each current, which is mapped in Fig. 6(a). Since a single cycle of frequency scanning takes almost 0.5 min, it is impossible to reconstruct the 50 Hz AC waveform by scanning the ODMR spectrum. Notably, we apply sinusoidal magnetic fields with amplitudes of 0.2 and 0.01 A, respectively, and record the ODMR spectra while scanning the current with a step of $\pi/100$ (corresponding to a time step of 100 μs), as plotted in Figs. 6(b) and 6(c). In this case, we can obtain two sets of resonant frequency series shown in Fig. 6(d), which are represented by f_- and f_+, respectively. It can be seen that the resonant frequency is almost linearly dependent on the magnetic field except for the

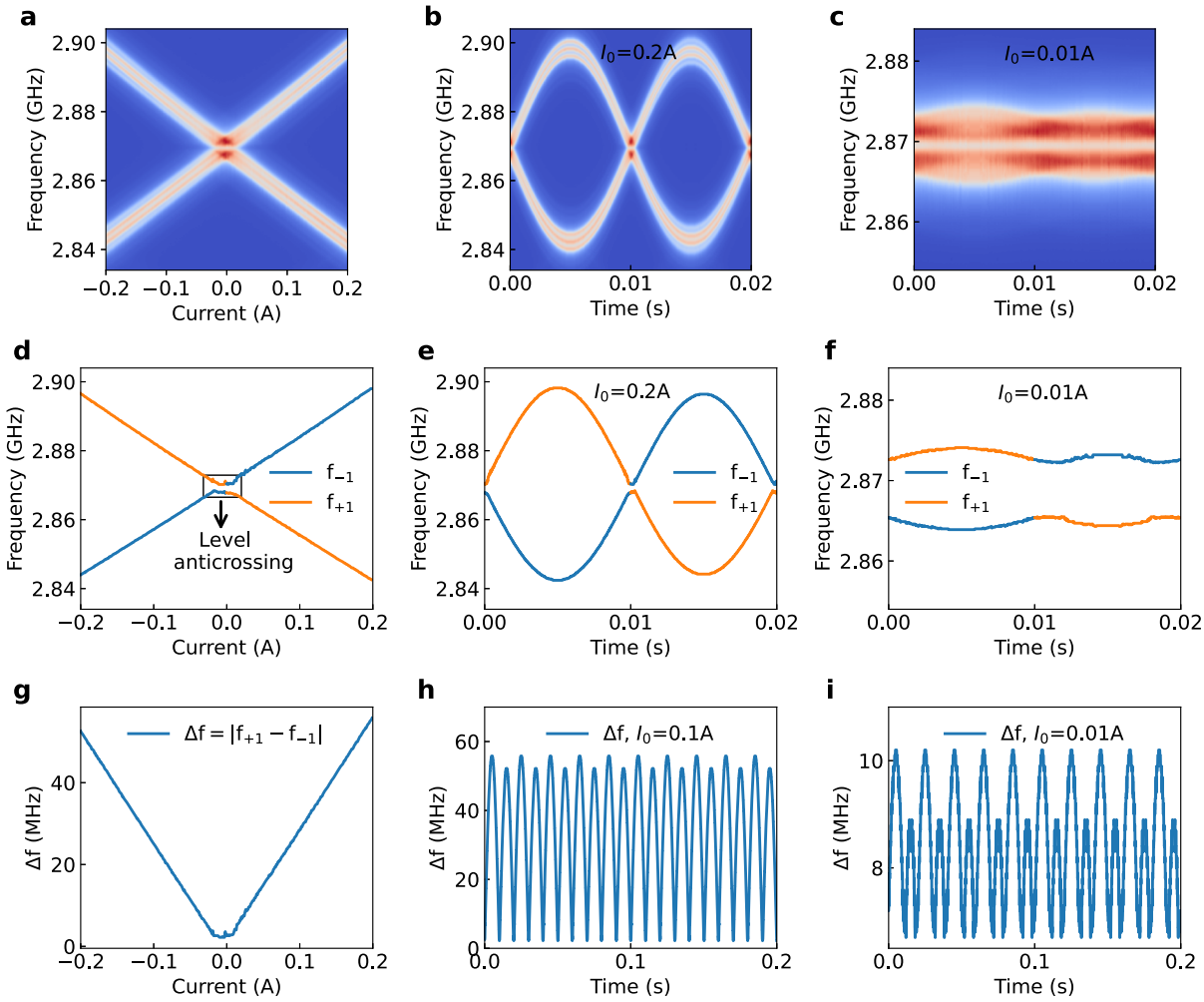

FIG. 6. Laboratory demonstration of the application of frequency tracking technology for AC magnetic field measurement. (a) ODMR spectra as a function of the magnetic field aligning along the [100] crystal direction. (b) and (c) ODMR spectra under one cycle of 50 Hz AC with amplitude I_0 of 0.2 and 0.01 A, respectively. (d)–(f). Resonance frequencies f_{-1} and f_{+1} extracted from (a)–(c). Level anti-crossing caused by transverse strain or electric field is marked by a black box in (a). It will significantly reduce the magnetic detection sensitivity of the under zero or weak magnetic field. (g) The resonant frequency difference $\Delta f = |f_{+1} - f_{-1}|$ of the two transitions ($|m_s = 0\rangle \rightarrow |m_s = -1\rangle$ and $|m_s = 0\rangle \rightarrow |m_s = +1\rangle$) is depicted in (d). This can suppress the influence of temperature variations on the current measurement accuracy. (h) and (i). Tracking the Δf for 0.2 s when applying a 50 Hz AC with amplitudes of 0.2 and 0.01 A, respectively.

near-zero field. Importantly, due to the stress and spin noise in diamonds, the zero-field ODMR exhibits a level anti-crossing (LAC) effect. This makes the diamond sensor extremely insensitive to weak magnetic field (low current) measurement. However, the LAC can be suppressed by purifying the ^{12}C isotope in diamond and optimizing the growth process.[46] Similarly, the resonant frequencies of Figs. 6(b) and 6(c) can also be extracted in Figs. 6(e) and 6(f).

Theoretically, the magnetic field can be obtained by $|f_+ - f_{-1}|/(2\gamma_e \cos\theta)$. This not only improves the magnetic field sensitivity by about 1.4 times but also suppresses the temperature drift.[47] However, the linearly polarized microwaves we use cannot distinguish between the two energy level transitions and cannot determine the positive and negative directions of the magnetic field. Ultimately, $|f_+ - f_-|$ is used as the magnetic field detection result, as shown in Fig. 6(g). To demonstrate frequency tracking within 0.2 s, we repeated $|f_+ - f_-|$ 10 times in Figs. 6(h) and 6(i), which is consistent with the plots in Fig. 2(d). The current measurement and calibration method introduced in Sec. II is still applicable to the current reconstruction based on frequency tracking technology.

APPENDIX C: DEMONSTRATION OF DUAL-FREQUENCY MICROWAVE FOR TEMPERATURE DRIFT SUPPRESSION

Since the zero-field splitting D_{zfs} in Eq. (2) is temperature-dependent, $dD_{zfs}/dt \approx -74$ kHz/K, making the two resonance fre-

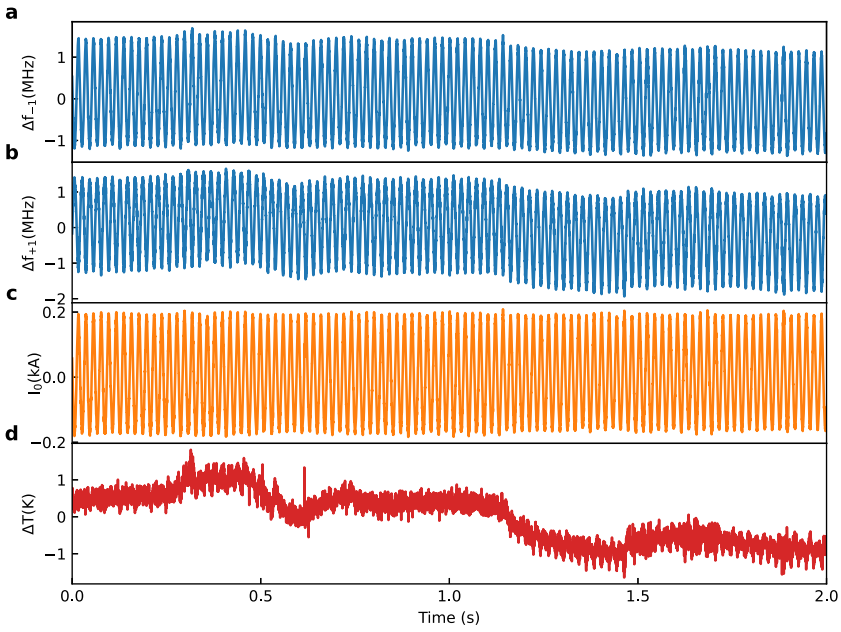

FIG. 7. Demonstration of dual-frequency technology for temperature drift suppression. (a) and (b) The measured magnetic field was obtained by tracking the two transitions f_{-1} and f_{+1} under a 50 Hz AC magnetic field. (c) and (d) Using the dual-frequency microwave detection method, the magnetic field and temperature can be decoupled. In this case, the temperature drift of the current measurement can be suppressed.

quencies f_{-1} and f_{+1} shift overall. Considering the variations in ambient temperature, these two resonant frequencies are given by

$$f_{\pm} = D_{\mathrm{zfs}}(T) + \Pi_z \pm \sqrt{\Pi_x^2 + \Pi_y^2 + (B_z + m_I A_{zz})^2}, \qquad \text{(C1)}$$

where $m_I = \{-1, 0, +1\}$. The temperature and magnetic field can be measured simultaneously by adding and subtracting f_{-1} and f_{+1}. By combining the current reconstruction algorithm introduced in Sec. II B with the frequency tracking technology in Appendix B, we use single-frequency and dual-frequency measurement methods to obtain the 50 Hz current time traces. When an AC is passed through the conductor, the current measurements obtained by tracking f_{-1} and f_{+1} for 2 s are shown in Figs. 7(a) and 7(b), respectively. Due to the temperature instability of the diamond caused by the laser heating effect, a significant temperature drift was observed in the current measurement. However, by $(f_{+1} - f_{-1})/2$, the current waveform becomes much smoother, showing the suppression of temperature drift, as shown in Fig. 7(c). In addition, by $(f_{+1} + f_{-1})/2$, the temperature of the sensor can be monitored synchronously, as shown in Fig. 7(d). Therefore, the dual-frequency tracking method of the diamond sensor can effectively suppress the temperature drift during current measurement, making QCT more reliable than the traditional commercially available current sensors. Generally, the measurement accuracy of commercial CTs does not exceed 0.2%, as shown in Table I. The QCT we developed can meet the requirements of power sites.

TABLE I. Performance comparison of different sensors.

Types	Range (kA)	Bandwidth (kHz)	Accuracy (%)	Temperature drift
SCT	1	100	0.2–1	Yes
Hall effect	0.5	1	0.5–5	Yes
Fluxgate	0.1	1	0.001–0.5	Yes
Fiber-optic	100	100	0.2–1	Yes
QCT	1	1.4	0.05–1	No.

REFERENCES

[1] K. Schon, *High Voltage Measurement Techniques* (Springer, 2019).
[2] T. Dake and E. Ozalevli, "A precision high-voltage current sensing circuit," IEEE Trans. Circuits Syst. I: Regular Pap. **55**, 1197–1202 (2008).
[3] D. Tzelepis, V. Psaras, E. Tsotsopoulou, S. Mirsaeidi, A. Dyśko, Q. Hong, X. Dong, S. M. Blair, V. C. Nikolaidis, V. Papaspiliotopoulos, G. Fusiek, G. M. Burt, P. Niewczas, and C. D. Booth, "Voltage and current measuring technologies for high voltage direct current supergrids: A technology review identifying the options for protection, fault location and automation applications," IEEE Access **8**, 203398–203428 (2020).
[4] F. Costa, P. Poulichet, F. Mazaleyrat, and E. Labouré, "The current sensors in power electronics, a review," EPE J. **11**, 7–18 (2001).
[5] R. M. Silva, H. Martins, I. Nascimento, J. M. Baptista, A. L. Ribeiro, J. L. Santos, P. Jorge, and O. Frazão, "Optical current sensors for high power systems: A review," Appl. Sci. **2**, 602–628 (2012).
[6] R. Weiss, R. Mattheis, and G. Reiss, "Advanced giant magnetoresistance technology for measurement applications," Meas. Sci. Technol. **24**, 082001 (2013).
[7] K. Schon, *High Impulse Voltage and Current Measurement Techniques* (Springer, 2013).
[8] C. Degen, F. Reinhard, and P. Cappellaro, "Quantum sensing," Rev. Mod. Phys. **89**, 035002 (2017).
[9] R. Kleiner, D. Koelle, F. Ludwig, and J. Clarke, "Superconducting quantum interference devices: State of the art and applications," Proc. IEEE **92**, 1534–1548 (2004).
[10] I. K. Kominis, T. W. Kornack, J. C. Allred, and M. V. Romalis, "A subfemtotesla multichannel atomic magnetometer," Nature **422**, 596–599 (2003).

[11]J. M. Taylor, P. Cappellaro, L. Childress, L. Jiang, D. Budker, P. R. Hemmer, A. Yacoby, R. Walsworth, and M. D. Lukin, "High-sensitivity diamond magnetometer with nanoscale resolution," Nat. Phys. **4**, 810–816 (2008).
[12]J. F. Barry, J. M. Schloss, E. Bauch, M. J. Turner, C. A. Hart, L. M. Pham, and R. L. Walsworth, "Sensitivity optimization for NV-diamond magnetometry," Rev. Mod. Phys. **92**, 015004 (2020).
[13]B. Fortman, L. Mugica-Sanchez, N. Tischler, C. Selco, Y. Hang, K. Holczer, and S. Takahashi, "Electron–electron double resonance detected NMR spectroscopy using ensemble NV centers at 230 GHz and 8.3 T," J. Appl. Phys. **130**, 083901 (2021).
[14]G.-Q. Liu, X. Feng, N. Wang, Q. Li, and R.-B. Liu, "Coherent quantum control of nitrogen-vacancy center spins near 1000 kelvin," Nat. Commun. **10**, 1344 (2019).
[15]C. Zhang, F. Shagieva, M. Widmann, M. Kübler, V. Vorobyov, P. Kapitanova, E. Nenasheva, R. Corkill, O. Rhrle, K. Nakamura, H. Sumiya, S. Onoda, J. Isoya, and J. Wrachtrup, "Diamond magnetometry and gradiometry towards subpicotesla dc field measurement," Phys. Rev. Appl. **15**, 064075 (2021).
[16]G. Chatzidrosos, A. Wickenbrock, L. Bougas, H. Zheng, O. Tretiak, Y. Yang, and D. Budker, "Eddy-current imaging with nitrogen-vacancy centers in diamond," Phys. Rev. Appl. **11**, 014060 (2019).
[17]J.-P. Tetienne, N. Dontschuk, D. A. Broadway, A. Stacey, D. A. Simpson, and L. C. L. Hollenberg, "Quantum imaging of current flow in graphene," Sci. Adv. **3**, e1602429 (2017).
[18]C. Feng, B.-W. Li, Y. Dong, X.-D. Chen, Y. Zheng, Z.-H. Wang, H.-B. Lin, W. Jiang, S.-C. Zhang, C.-W. Zou, G.-C. Guo, and F.-W. Sun, "Quantum imaging of the reconfigurable VO_2 synaptic electronics for neuromorphic computing," Sci. Adv. **9**, eadg9376 (2023).
[19]J. F. Barry, M. J. Turner, J. M. Schloss, D. R. Glenn, Y. Song, M. D. Lukin, H. Park, and R. L. Walsworth, "Optical magnetic detection of single-neuron action potentials using quantum defects in diamond," Proc. Natl. Acad. Sci. U. S. A. **113**, 14133–14138 (2016).
[20]J. L. Webb, L. Troise, N. W. Hansen, J. Achard, O. Brinza, R. Staacke, M. Kieschnick, J. Meijer, J.-F. Perrier, K. Berg-Sørensen, A. Huck, and U. L. Andersen, "Optimization of a diamond nitrogen vacancy centre magnetometer for sensing of biological signals," Front. Phys. **8** (2020).
[21]Q. Liu, F. Xie, X. Peng, Y. Hu, N. Wang, Y. Zhang, Y. Wang, L. Li, H. Chen, J. Cheng, and Z. Wu, "Millimeter-scale temperature self-calibrated diamond-based quantum sensor for high-precision current sensing," Adv. Quantum Technol. **6**, 2300210 (2023).
[22]Z.-Y. Shi, W. Gao, Q. Wang, H. Guo, J. Tang, Z.-H. Li, H.-F. Wen, Z.-M. Ma, and J. Liu, "Current sensor based on diamond nitrogen-vacancy color center," Chin. Phys. B **32**, 070704 (2023).
[23]Q. Liu, F. Xie, X. Peng, Y. Zhang, N. Wang, Y. Hu, L. Wang, Y. Liu, Y. Wang, S. Nie, H. Chen, J. Cheng, and Z. Wu, "Closed-loop diamond quantum sensor for large range and high precision current measurement," IEEE Sens. J. **24**, 4356–4364 (2024).
[24]Y. Hatano, J. Shin, J. Tanigawa, Y. Shigenobu, A. Nakazono, T. Sekiguchi, S. Onoda, T. Ohshima, K. Arai, T. Iwasaki, and M. Hatano, "High-precision robust monitoring of charge/discharge current over a wide dynamic range for electric vehicle batteries using diamond quantum sensors," Sci. Rep. **12**, 13991 (2022).
[25]L. Q. Zhou, R. L. Patel, A. C. Frangeskou, A. Nikitin, B. L. Green, B. G. Breeze, S. Onoda, J. Isoya, and G. W. Morley, "Imaging damage in steel using a diamond magnetometer," Phys. Rev. Appl. **15**, 024015 (2021).
[26]R. L. Patel, L. Q. Zhou, A. C. Frangeskou, G. A. Stimpson, B. G. Breeze, A. Nikitin, M. W. Dale, E. C. Nichols, W. Thornley, B. L. Green, M. E. Newton, A. M. Edmonds, M. L. Markham, D. J. Twitchen, and G. W. Morley, "Subnanotesla magnetometry with a fiber-coupled diamond sensor," Phys. Rev. Appl. **14**, 044058 (2020).
[27]S. M. Graham, A. T. M. A. Rahman, L. Munn, R. L. Patel, A. J. Newman, C. J. Stephen, G. Colston, A. Nikitin, A. M. Edmonds, D. J. Twitchen, M. L. Markham, and G. W. Morley, "Fiber-coupled diamond magnetometry with an unshielded sensitivity of 30 $30\text{pT}/\sqrt{\text{hz}}$," Phys. Rev. Appl. **19**, 044042 (2023).
[28]S.-C. Zhang, H.-B. Lin, Y. Dong, B. Du, X.-D. Gao, C. Yu, Z.-H. Feng, X.-D. Chen, G.-C. Guo, and F.-W. Sun, "High-sensitivity and wide-bandwidth fiber-coupled diamond magnetometer with surface coating," Photonics Res. **10**, 2191–2201 (2022).
[29]S.-C. Zhang, Y. Liu, L.-K. Shan, X.-D. Gao, J.-Q. Geng, C. Yu, Y. Dong, X.-D. Chen, G.-C. Guo, and F.-W. Sun, "Picotesla fiberized diamond-based AC magnetometer," Photonics Res. **12**, 1250–1261 (2024).
[30]H. Zheng, J. Xu, G. Z. Iwata, T. Lenz, J. Michl, B. Yavkin, K. Nakamura, H. Sumiya, T. Ohshima, J. Isoya, J. Wrachtrup, A. Wickenbrock, and D. Budker, "Zero-field magnetometry based on nitrogen-vacancy ensembles in diamond," Phys. Rev. Appl. **11**, 064068 (2019).
[31]P. London, P. Balasubramanian, B. Naydenov, L. P. McGuinness, and F. Jelezko, "Strong driving of a single spin using arbitrarily polarized fields," Phys. Rev. A **90**, 012302 (2014).
[32]C. Wang, Q. Liu, Y. Hu, F. Xie, K. Krishna, N. Wang, L. Wang, Y. Wang, K. C. Toussaint, J. Cheng, H. Chen, and Z. Wu, "Realization of high-dynamic-range broadband magnetic-field sensing with ensemble nitrogen-vacancy centers in diamond," Rev. Sci. Instrum. **94**, 015109 (2023).
[33]H. Clevenson, L. M. Pham, C. Teale, K. Johnson, D. Englund, and D. Braje, "Robust high-dynamic-range vector magnetometry with nitrogen-vacancy centers in diamond," Appl. Phys. Lett. **112**, 252406 (2018).
[34]A. M. Wojciechowski, M. Karadas, C. Osterkamp, S. Jankuhn, J. Meijer, F. Jelezko, A. Huck, and U. L. Andersen, "Precision temperature sensing in the presence of magnetic field noise and vice-versa using nitrogen-vacancy centers in diamond," Appl. Phys. Lett. **113**, 013502 (2018).
[35]Y. Hatano, J. Shin, D. Nishitani, H. Iwatsuka, Y. Masuyama, H. Sugiyama, M. Ishii, S. Onoda, T. Ohshima, K. Arai, T. Iwasaki, and M. Hatano, "Simultaneous thermometry and magnetometry using a fiber-coupled quantum diamond sensor," Appl. Phys. Lett. **118**, 034001 (2021).
[36]D. Kim, M. I. Ibrahim, C. Foy, M. E. Trusheim, R. Han, and D. R. Englund, "A CMOS-integrated quantum sensor based on nitrogen–vacancy centres," Nat. Electron. **2**, 284–289 (2019).
[37]K. Omirzakhov, M. H. Idjadi, T.-Y. Huang, S. A. Breitweiser, D. A. Hopper, L. C. Bassett, and F. Aflatouni, "An integrated quantum spin control system in 180nm CMOS," in *2022 IEEE Radio Frequency Integrated Circuits Symposium (RFIC)* (IEEE, 2022), pp. 43–46.
[38]S. Esmaeili, P. Schmalenberg, S. Wu, Y. Zhou, S. Rodrigues, N. Hussain, T. Kimura, Y. Tadokoro, S. Higashi, D. Banerjee, and E. M. Dede, "Evolution of quantum spin sensing: From bench-scale ODMR to compact integrations," APL Mater. **12**, 040901 (2024).
[39]J. Song, G. Zhang, Y. Nie, G. Wang, H. Li, and Y. Hou, "Design and simulation of a magnetic balance weak current sensor based on TMR," J. Phys.: Conf. Ser. **1617**, 012038 (2020).
[40]J. Yu, Z. Long, S. Liang, C. Yue, X. Yin, and F. Zhou, "Optimal design of dual air-gap closed-loop TMR current sensor based on minimum magnetic field uniformity coefficient," Sci. Rep. **13**, 239 (2023).
[41]H. Zhang, F. Li, H. Guo, Z. Yang, and N. Yu, "Current measurement with 3-D coreless TMR sensor array for inclined conductor," IEEE Sens. J. **19**, 6684–6690 (2019).
[42]X. P. Xu, L. X. Yang, H. Y. Chen, T. Z. Liu, X. L. Xu, Z. Sun, and H. L. Liu, "Traction network wire current detection based on ring-shaped TMR array," IEEE Trans. Transp. Electrif. **10**, 4268–4278 (2024).
[43]S. Maayani, C. Foy, D. Englund, and Y. Fink, "Distributed quantum fiber magnetometry," Laser Photonics Rev. **13**, 1900075 (2019).
[44]E. Bauch, S. Singh, J. Lee, C. A. Hart, J. M. Schloss, M. J. Turner, J. F. Barry, L. M. Pham, N. Bar-Gill, S. F. Yelin, and R. L. Walsworth, "Decoherence of ensembles of nitrogen-vacancy centers in diamond," Phys. Rev. B **102**, 134210 (2020).
[45]K. Sasaki, Y. Monnai, S. Saijo, R. Fujita, H. Watanabe, J. Ishi-Hayase, K. M. Itoh, and E. Abe, "Broadband, large-area microwave antenna for optically detected magnetic resonance of nitrogen-vacancy centers in diamond," Rev. Sci. Instrum. **87**, 053904 (2016).
[46]T. Mittiga, S. Hsieh, C. Zu, B. Kobrin, F. Machado, P. Bhattacharyya, N. Z. Rui, A. Jarmola, S. Choi, D. Budker, and N. Y. Yao, "Imaging the local charge environment of nitrogen-vacancy centers in diamond," Phys. Rev. Lett. **121**, 246402 (2018).
[47]I. Fescenko, A. Jarmola, I. Savukov, P. Kehayias, J. Smits, J. Damron, N. Ristoff, N. Mosavian, and V. M. Acosta, "Diamond magnetometer enhanced by ferrite flux concentrators," Phys. Rev. Res. **2**, 023394 (2020).